Experimental investigation of circumnutation-inspired penetration in sand

To cite this article before publication: Riya Anilkumar *et al* 2024 *Bioinspir. Biomim.* in press https://doi.org/10.1088/1748-3190/ad8c89

IOP Publishing Journal Title
Journal **XX** (XXXX) XXXXXX https://doi.org/XXXX/XXXX

Experimental Investigation of Circumnutation-Inspired Penetration in Sand

Riya Anilkumar[1], Alejandro Martinez[1]

[1] Department of Civil and Environmental Engineering, University of California Davis, Davis, USA

E-mail: ranilkumar@ucdavis.edu

Received xxxxxx
Accepted for publication xxxxxx
Published xxxxxx

Abstract

Probes that penetrate soil are used in fields such as geotechnical engineering, agriculture, and ecology to classify soils and characterize their properties *in situ*. Conventional tools such as the Cone Penetration Test (CPT) often face challenges due to the lack of reaction force needed to penetrate stiff or dense soil layers, necessitating the use of large drill rigs. This paper investigates more efficient means of penetrating soil by taking inspiration from a plant-root motion known as circumnutation. Experimental penetration tests on sands are performed with circumnutation-inspired (CI) probes that advance at a constant vertical velocity (v) while simultaneously rotating at a constant angular velocity (ω). These probes have bent tips with a given bent angle (α) and bent length (L_1). The variation of the mobilized vertical force (F_z), torque (T_z), and the mechanical work components with the relative tangential to vertical velocity ($\omega R/v$, where R is the distance of the tip of the probe from the vertical axis of rotation) is investigated along with the effects of probe geometry, vertical velocity, and soil relative density (D_R). The results show that the soil penetration resistance does not vary with v, but it increases as α, L_1, and D_R are increased. F_z decays exponentially with increasing $\omega R/v$, T_z initially increases and then plateaus, while total work (W_T) shows little magnitude changes initially but later increases monotonically. The mechanisms leading to these trends are identified as the changes in the probe projected areas and mobilized normal stresses due to differences in probe geometry and the effects of $\omega R/v$ on the resultant force direction and soil disturbance. The results show that CI penetration within a specific range of $\omega R/v$ leads to small increases in W_T (i.e., $\leq$ 25%), yet mobilizes F_z magnitudes that are 50 to 80% lower than that mobilized during non-rotational penetration. This indicates that CI penetration can be adopted for *in situ* characterization or sensor placement with smaller vertical forces, allowing for use of lighter rigs.

Keywords: soil penetration, burrowing, circumnutations, plant roots

IOP Publishing Journal Title
Journal **XX** (XXXX) XXXXXX https://doi.org/XXXX/XXXX

1. Introduction

Soil penetration is an important aspect of subsurface exploration for various applications such as geotechnical engineering, agriculture, ecology, natural and anthropogenic hazard assessment, and space exploration. Soil penetrometers are used in agriculture to estimate soil moisture content, density, compaction, composition, crop yield, tillage, and mobility of wheels and crawler tracks in fields (Campbell and O'Sullivan, 1991; Davidson, 1965; Moraes et al., 2014). Ecological soil conditions are also monitored using penetrometers and sensors buried in soil to evaluate parameters such as moisture content, contamination presence, and temperature (Guireli Netto et al., 2020; Robinson et al., 2008). Another major application is geotechnical soil characterization for construction of roads, tunnels, excavations, and foundations and for installation of sensors for continued monitoring of infrastructure such as dams and embankments (Abdoun et al., 2005; Mayne, 2007; Simons et al., 2002; Wan and Standing, 2014). Geotechnical *in situ* testing methods, such as the Cone Penetration Test (CPT), Dilatometer Test (DMT), and Standard Penetration Test (SPT), require large reaction forces to penetrate through stiff or deep layers of soil (Huang and Ma, 1994; Jamiolkowski et al., 2012; Schmertmann and Palacios, 1979). Therefore, rigs used for these tests typically have large sizes and reaction masses to enable penetration. These attributes can pose challenges due to the increased cost and carbon footprint of mobilization of the equipment (Purdy et al., 2022; Raymond et al., 2020; Shillaber et al., 2014) and to difficulties in reaching sites with limited accessibility, such as environmentally protected regions, dense urban areas, and underneath existing structures. Use of soil penetration strategies that reduce the penetration resistance would allow using smaller-sized and lighter equipment, resulting in lower mobilization costs and environmental impacts and enabling characterization of sites that are difficult to reach, such as outer space bodies.

Soil penetration is also a common process involved in the growth and survival of plants and animals that has evolved over millions of years to achieve greater efficiency. Different organisms have developed adaptations that aid their needs in different soil environments. Some animals use undulating body motions to burrow, such as the polychaetes (Dorgan et al., 2013), oigochaetes (Kudrolli and Ramirez, 2019), sandfish lizards (Maladen et al., 2009), and sand lances (Gidmark et al., 2011). Razor clams use a dual anchor strategy (Trueman, 1967; Winter and Hosoi, 2011) and marine and earth worms use peristalsis (Dorgan, 2018). Plant roots have been reported to grow laterally to decrease the penetration resistance when they encounter a stiff layer (e.g., Bengough et al., 1994). In these strategies, radial expansion of a segment near the tip results in either crack propagation (Dorgan et al., 2005) or stress relaxation (Chen et al., 2021; Shin and Santamarina, 2011) to decrease the penetration resistance.

Plant roots also exhibit a different type of motion that has been reported to aid in soil penetration called circumnutations. During circumnutations, an irregular helical shape is traced by the root tip as it penetrates the soil. This motion has been hypothesized to have both endogenous (autonomous, dictated by internal rhythms) and exogenous (effected by external factors or stimuli) origins for reduction in vertical resistance to penetration and obstacle avoidance (Darwin and Darwin, 1880; Kiss, 2009; Loshchilov et al., 2021; Millar et al., 2011; Taylor et al., 2021). The helical (irregular) trajectory of root tip paths is clearly observed in some plant species; however, the roots straighten out in others (Migliaccio et al., 2013). Due to this being an autonomous and universal motion of plants, it is observed in different soils that vary in composition, moisture content, and depth.

Taking inspiration from these biological mechanisms can help develop more efficient means of penetrating soil. Bio-inspiration for soil penetration is an area that has received significant attention in recent years (Martinez et al., 2022; Del Dottore et al., 2017). Experimental and numerical investigations on probes inspired by earthworms, razor clams, and polychaetes showed that radial expansion aids in soil penetration by providing anchorage and reducing the penetration resistance (Chen et al., 2021; Dorgan, 2018; Huang and Tao, 2020; Martinez et al., 2020; Naziri et al., 2021). Some studies developed probes that penetrate soil by using additive structures near the tip, mimicking root tip growth and thus reducing the penetration force as well as the total energy consumption (Sadeghi et al., 2014). Del Dottore et al. (2017) and Chen and Martinez (2024) performed experimental and numerical investigations of a probe that uses circumnutation-inspired (CI) motion to penetrate soil, showing a reduction in vertical resistance with increasing angular velocity along with a small reduction in the total work done for penetration. The study by Del Dottore et al. (2017) explored different sand densities and observed similar trends of variation of force and total work with increasing angular velocity of motion. Chen and Martinez (2024) also showed that the relative velocity of the probe, defined as the ratio of tangential to vertical velocity ($\omega R/v$), is a governing parameter controlling the magnitude of force, torque, and work done during CI penetration. These previous works have shown that while the probe geometry, magnitude of vertical and angular velocities, and soil density play a role in the variation of resistance and work, the mechanisms that result in these

IOP Publishing Journal Title
Journal **XX** (XXXX) XXXXXX https://doi.org/XXXX/XXXX

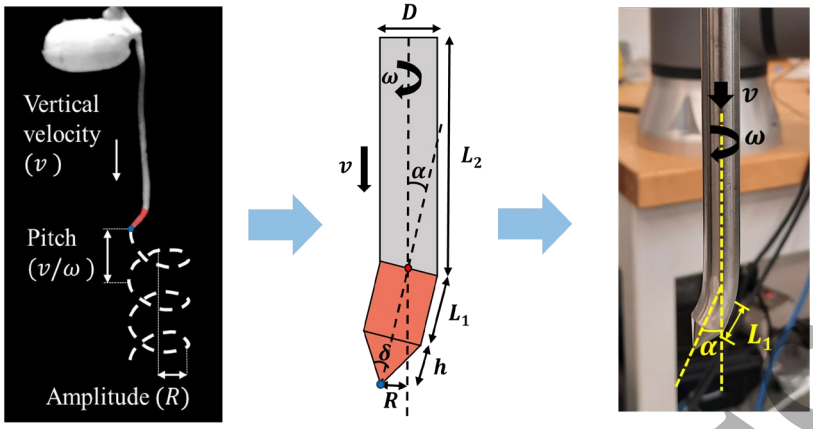

Inspiration (modified from Taylor et al., 2021) | Idealized probe design | Fabricated bio-inspired probe

Figure 1: Design of bio-inspired probe

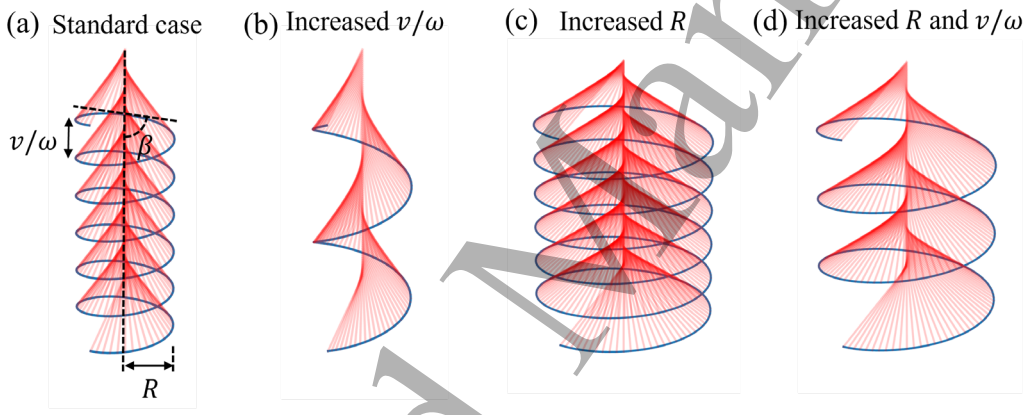

Figure 2: Helical trajectory of the tip of the probe (indicated as a red line with a blue tip end) and its variation with changes in R and v/ω. Helix slope $tan(\beta) = \omega R/v$. Case (a) depicts an example helical trajectory with helix pitch v/ω, radius (R) and helix angle (β). Case (b) shows a decrease in β as v/ω is increased, case (c) shows an increase in β as R is increased, and case (d) shows no change in β as both v/ω and R are increased proportionally.

variations and their dependence on these parameters are still not fully understood.

This study aims to further the understanding of the underlying mechanisms resulting in the variations of force, torque, and work during CI penetration. This work explores the effect of the probe geometry, penetration velocity, and soil density on the measured responses. Different probe geometries and penetration relative velocities which have not been previously reported in the literature are explored in the study. This paper quantifies the changes in the mobilized resistances as the test parameters are varied, and provides discussion on the factors controlling them. It also provides guidance on the use of CI penetration to reduce the vertical penetration force (F_z) with small impacts to the total cumulative work (W_T) done to enable efficient soil penetration in the field.

2. Bio-inspiration and methods of investigation

The circumnutation motion and its parameters vary in different plant species and environments (Chen and Martinez, 2024). Plant root tips are often bent and during circumnutation the direction of the tip growth rotates as the root grows in the soil (Mullen et al., 1998). The diameter of the root (D), bent angle (α), length of the bent tip (L_1), rate of vertical penetration (v), and angular velocity (ω) are circumnutation parameters that vary in different plant species.

IOP Publishing Journal Title
Journal **XX** (XXXX) XXXXXX https://doi.org/XXXX/XXXX

The root can be idealized as a straight cylindrical probe with a bent conical tip that rotates with a given ω and vertically penetrates the soil with a given v. Based on this, the CI penetration probe for experimental investigation was fabricated by bending the tip of a straight cylindrical probe with a conical end (like a CPT probe), as shown in Figure 1. The angle at which the tip is bent is given by α and the distance between the central point of curvature of the bend and the start of the conical end of the probe tip, which depicts the bent length of the tip, is given by L_1 (Figure 1). The trajectory of the tip can be idealized as a regular helix whose pitch is v/ω and the slope of the helix is $tan(\beta) = \omega R/v$ (Figure 2a), where the trajectory of the probe tip is shown in blue and different locations of the bent length are shown in red. The radius of the helix (R) is determined by L_1 and α, where $R = L_1 sin(\alpha)$. Figures 2b-2d shows variations in the probe tip trajectory with variations in v/ω and R. While plant roots have varying sizes, the CI penetration probes used for the investigation have a fixed diameter of 12.7 mm. A conical apex angle (δ) of 60° is used, which is the standard for CPT probes used in geotechnical engineering. The probes are fabricated from stainless steel and have a smooth surface.

The probe geometry and penetration motions were inspired by those of plant roots reported in the literature, as summarized in Chen and Martinez (2024), based on the measurements from Del Dottore et al. (2017), Kim et al. (2016), Mullen et al. (1998), Popova et al. (2012), Simmons et al. (1995), and Taylor et al. (2021). The probes have L_1 ranging from $1D$ to $3D$ and α ranging from 10° to 30°, in comparison to L_1 ranging from $2D$ to $7D$ and α ranging from 2° to 45° in plants. The range of vertical velocity used in this study is much higher than those observed in plants to complete the experiments in a reasonable time. Namely, the experiments are performed at velocities between 0.1 and 0.5 mm/s while plant growth rate has been reported in the range between 1 and 50 mm/day. However, the $\omega R/v$ of the probe tip used in this study ranges from 0.0 to 4.0 π, which is similar to the range of 0.2 to 2.0 π observed in plant roots.

The experimental setup consists of a UR16e robotic arm (Universal Robots) with the NET six-axis load cell (ATI Industrial Automation) onto which a stepper motor (Teknic ClearPath NEMA 23) and a gearbox (Carson Manufacturing S-Series Planetary) are mounted, and the probe is then attached to the gearhead (Figure 3a). The robotic arm is used to push the probe at v, while the motor and gearbox rotate the probe at ω and the load cell measures the F_z and torque along the vertical axis (T_z) generated during penetration.

All the penetration tests were performed in dry sand deposits with uniform densities. Deposits with target relative densities ($D_R = (e_{max} - e)/(e_{max} - e_{min})$, where e_{max} and e_{min} are the void ratios of the soil at the loosest and densest states, respectively, as described in ASTM D 653-03) of 40% ($\rho = 1.48\ g/cc$) and 70% ($\rho = 1.56\ g/cc$) were prepared. These states have porosities of 0.432 and 0.401, respectively. The uniform sand deposits were prepared using the air pluviation method, a widely used laboratory method for the preparation of uniform cohesionless soil deposits where sand is rained in layers using a pluviator while maintaining a fixed drop height

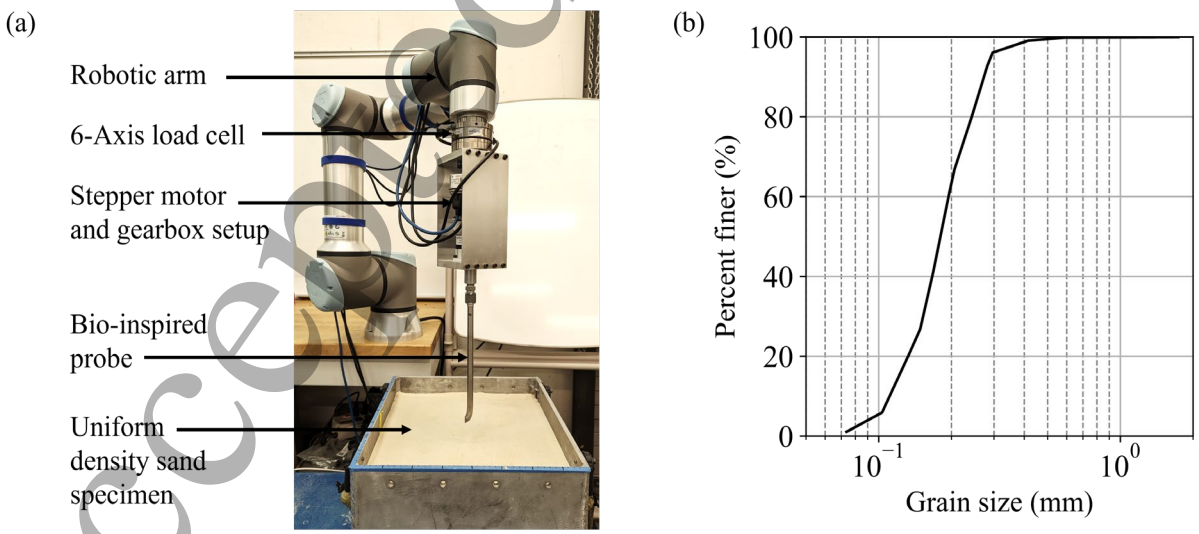

Figure 3: (a) Experimental setup of CI penetration with components of the setup labeled. (b) Grain size distribution of 100A sand used for experimental investigation

IOP Publishing Journal Title
Journal **XX** (XXXX) XXXXXX https://doi.org/XXXX/XXXX

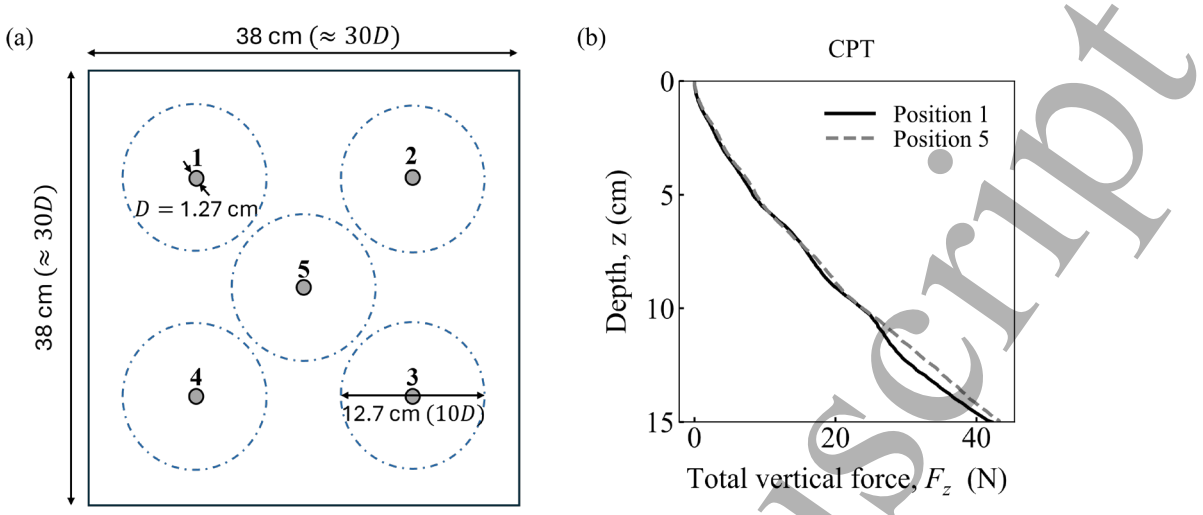

Figure 4: (a) Schematic of the order and positions of testing in one prepared sand deposit. The smaller diameter grey circles indicate the probe (diameter = $1D$) and the blue dashed lined larger circle indicates the expected zone of influence of $10D$ in diameter. (b) The variation of F_z with depth between a CPT test performed in position 1 located in one corner of the container and a second CPT performed in position 5 in the centre of the same container.

(Vaid and Negussey, 1988). A 20 cm deep deposit was prepared in ten layers. The depth of the deposit is greater than the depth of penetration during testing by $4D$. Based on extrapolation from the sensing distance chart by Boulanger and DeJong (2018), it was estimated that the increase in the measured F_z due to the rigid base of the container will be small (<5%) at this spacing. The sand used was a uniform sub-angular quartz sand (referred to as 100A sand in Ahmed et al., 2023). It has a median particle size (D_{50}) of 0.18 mm, 10th percentile particle size (D_{10}) of 0.12 mm, coefficient of uniformity (C_u) of 1.74, coefficient of curvature (C_c) of 1.04, and critical state friction angle (φ'_{cs}) determined from triaxial tests of 32.1°. Figure 3b shows the sand's grain size distribution.

Different test sets were performed at $\omega R/v$ ranging from 0 π to 4 π where D_R, α, L_1, and v were varied one at a time, as shown in Table 1. CPT soundings were also performed for comparison in the loose and dense soil deposits using CPT probes with the same diameter and apex angle as the CI penetration probes. Four to five penetration tests are performed in each deposit (container dimensions = 38 cm × 38 cm ≈ $30D \times 30D$, as illustrated in Figure 4a) where each penetration test is performed at a spacing of $10D$ to $12D$ from each other and from the walls of the container, which has been shown to avoid disturbance and boundary effects by Bolton et al., 1999. This distance between tests was further found to be appropriate based on CPT tests performed in the central and corner test position in the deposit mobilize similar vertical resistance (Figure 4b). Once a set of five tests is performed, a new deposit of sand is pluviated for the next set. To ensure consistency in the density of the prepared deposits, CPTs were performed in different deposits with D_R of 40% and 70%, indicated a of variability of 5% to 10% from mean at depths greater than 5 cm (Figure 5a-b). The variability in the F_z measurements was assessed by performing eight duplicate CI tests with various configurations. The variability was less than 2.2 N in the loose sand deposits and 3 N in the dense sand deposits. Overall, this yields a variation of 3-15% from mean. The variability in measured T_z was also found to be small, under 0.01 Nm for most tests, but reaching values as high as 0.03 Nm for two tests at $\omega R/v$ of 4 π. Any differences in the data within this range is considered to be due to the variability between tests, rather than due to changes in probe geometry or testing parameters.

IOP Publishing Journal Title
Journal **XX** (XXXX) XXXXXX https://doi.org/XXXX/XXXX

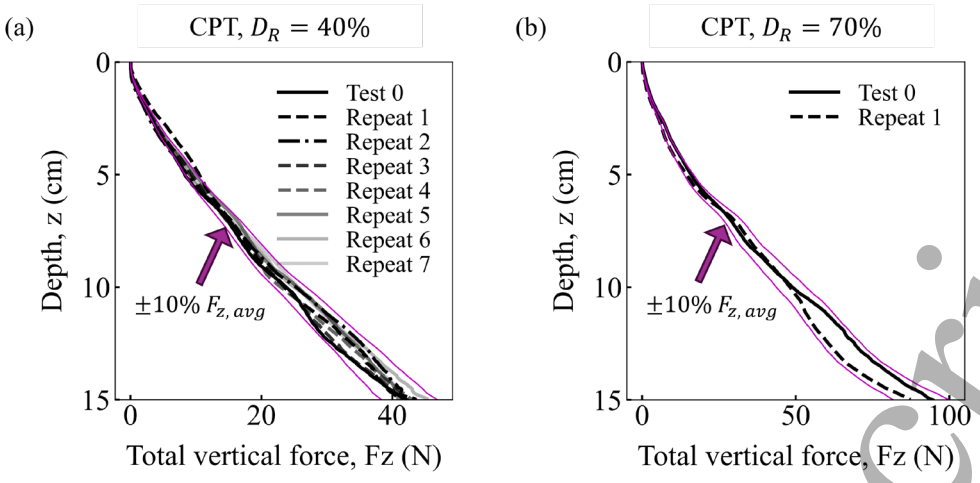

Figure 5: Variation of F_z with depth for CPT tests in (a) $D_R = 40\%$ and (b) $D_R = 70\%$ sand deposits, highlighting the variability between repeated tests.

Table 1: Test sets with the parameter varied with respect to the reference set. The parameters modified in each test are highlighted in bold font. *Note that for an α of 0° (straight probe), R is zero by definition, thus $\omega R/v$ is always zero for this probe.

Test Parameter	**$\omega R/v$ (π)**	**ω (RPM)**	**v (mm/s)**	**α**	**L_1**	**Target D_R**
Reference	0, 0.25, 0.5, 1, 2, 4	0, 0.9, 1.8, 3.6, 7.3, 14.6	0.5	10°	1D	40
Effect of L_1	0, 0.25, 0.5, 1, 2, 4	0, 0.4, 0.9, 1.8, 3.5, 7.0	0.5	10°	**3D**	40
Effect of α	0*	0, 0.9, 1.8, 3.6, 7.3, 14.6	0.5	**0°**	1D	40
	0, 0.25, 0.5, 1, 2, 4	0, 0.5, 0.9, 1.8, 3.7, 7.4	0.5	**20°**	1D	40
	0, 0.25, 0.5, 1, 2, 4	0, 0.3, 0.6, 1.3, 2.6, 5.1	0.5	**30°**	1D	40
Effect of D_R	0, 0.25, 0.5, 1, 2, 4	0, 1.8, 3.6, 7.3, 14.6	0.5	10°	1D	**70**
Effect of v	0, 0.25, 0.5, 1, 2, 4	0, 0.18, 0.36, 0.73, 1.46, 2.92	**0.1**	10°	1D	40
	0.12, 0.25, 0.5, 1, 2, 4	2.92	**0.1, 0.2, 0.4, 0.8, 1.6, 3.3**	10°	1D	40

3. Results

3.1 Reference test: variation with relative velocity

The reference set of tests with fixed test parameters (L_1 =1D, α = 10°, D_R = 40%, v = 0.5 mm/s) and varying ω is performed to investigate the effects of $\omega R/v$ on the force, torque, and work done during CI penetration. The F_z and T_z mobilized during CI penetration increase monotonically with depth. The mobilized F_z decreases substantially as $\omega R/v$ is increased (Figure 6a). The T_z increases from negligible values for the non-rotating probes (i.e., 0.0 π) to higher magnitudes with initial increase in $\omega R/v$, but shows little changes with further increases (Figure 6b). The above-mentioned trends of variation of F_z and T_z with $\omega R/v$ are consistent at all depths. The figures also include the results of a test with a CPT probe (i.e., non-rotational probe without a bend), showing that it mobilizes the greatest F_z and negligible T_z.

Given the consistency of F_z and T_z trends with depth, the average F_z and T_z values across the entire depth of penetration are considered to examine the variation with $\omega R/v$. The average F_z calculated over the entire penetration depth (i.e., 0 to 15 cm) exponentially decreases with increasing $\omega R/v$ (Figure 7a). The average T_z increases considerably with an initial increase in $\omega R/v$, while further increases yield a modest reduction followed by limited change in the magnitude (Figure 7b).

The cumulative vertical (W_V) and rotational work (W_R) done to penetrate a certain depth have contrasting trends with increasing $\omega R/v$, where W_V decreases and W_R increases. Cumulative vertical work and rotational work are computed from F_z and T_z as the incremental sum of the product of F_z and T_z with the corresponding vertical and rotational displacements through the depth of penetration, while the total work is defined as the sum of W_V and W_R, as follows:

$$W_V = \sum_{d_i}^{d_f} F_z v \Delta t \quad (1)$$

$$W_R = \sum_{d_i}^{d_f} T_z \omega \Delta t \quad (2)$$

$$W_T = W_V + W_R \quad (3)$$

where d_i is the initial depth, d_f is the final depth, and Δt is the time difference between subsequent data points.

The W_V and W_R increase with depth, but their variation with $\omega R/v$ are consistent (Figures 6c-d). Figure 7c presents the calculated W_V, W_R, and W_T done to penetrate to a depth of 15 cm. As shown, W_V exponentially decays, W_R monotonically increases, and W_T has small variations

IOP Publishing Journal Title
Journal **XX** (XXXX) XXXXXX https://doi.org/XXXX/XXXX

in magnitude with initial increments in $\omega R/v$ but increases steadily with further increases in $\omega R/v$. Since all the tests in the reference set were performed at a constant vertical velocity and depth of penetration, W_V follows the same trends as the average F_z. While the T_z magnitudes vary from about 0.03 to 0.05 Nm for different non-zero $\omega R/v$, increasing ω govern the increase in W_R due to the increase in rotational displacement (i.e., $\omega \Delta t$). The variation of W_T with $\omega R/v$ is governed by the variation of W_V and W_R, where the influence of W_V decreases as $\omega R/v$ is increased while the influence of W_R steadily increases. The initial stagnation of the magnitude of W_T with small increases in $\omega R/v$ is due to the similar absolute rate of change in W_V and W_R with increasing $\omega R/v$.

The trade-off between increasing W_T and decreasing F_z can be analyzed by comparing the changes in these quantities

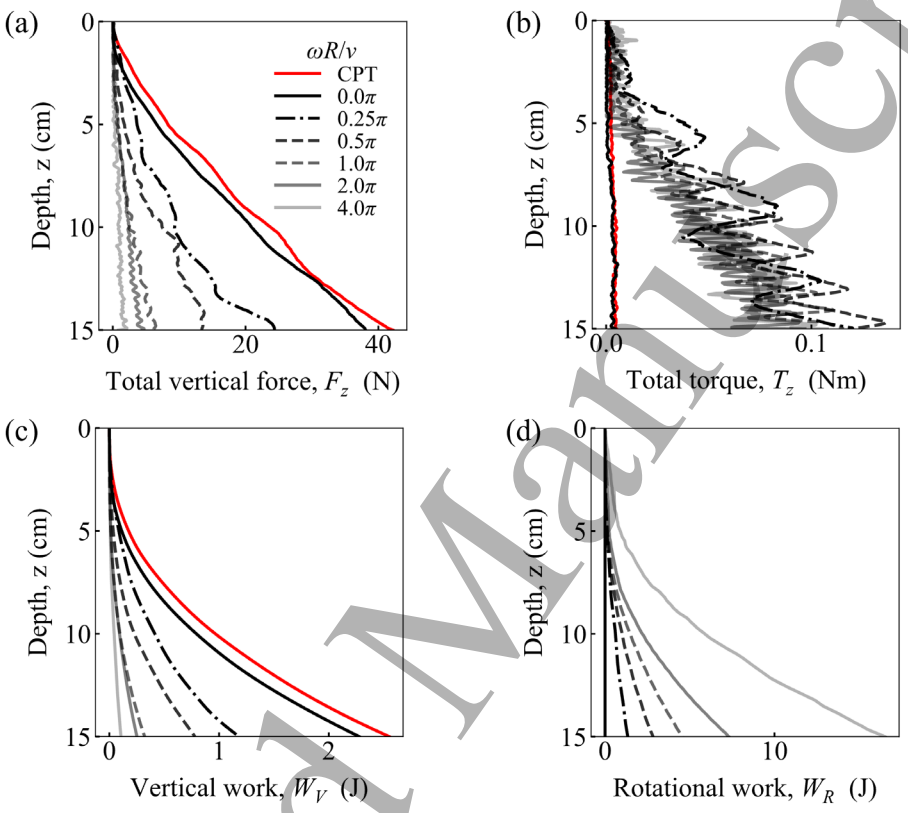

Figure 6: Variation with depth for (a) vertical force, (b) torque, (c) vertical work, and (d) rotational work

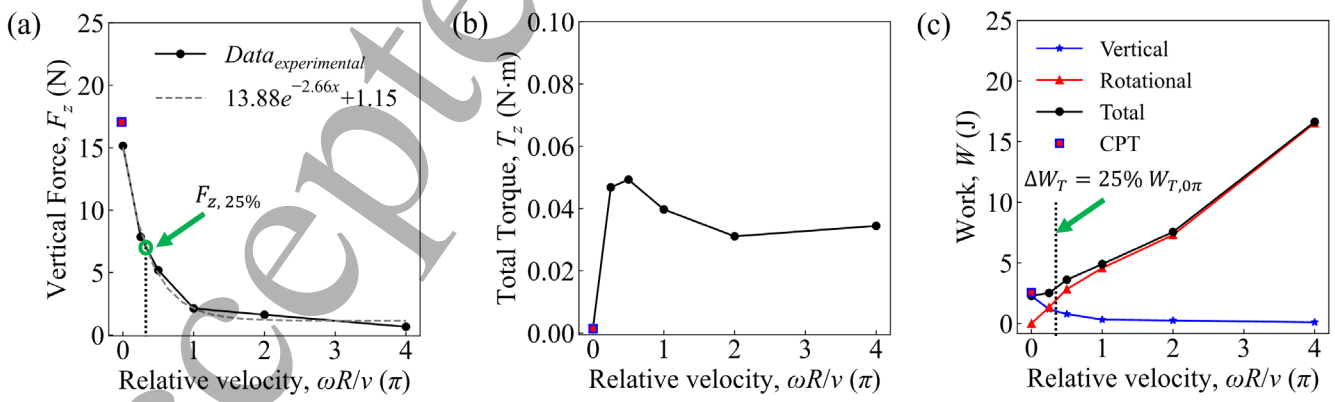

Figure 7: Variation of (a) depth-averaged vertical force, (b) depth-averaged torque, and (c) cumulative work with relative velocity of penetration for probe with L_1= 1D, α =10° in 40% D_R sand (reference set of tests). Dotted lines indicating the $\omega R/v$ at which total work increases by 25% in comparison to non-rotational CIM tests are marked to highlight the extent of decay in vertical force.

IOP Publishing Journal Title
Journal **XX** (XXXX) XXXXXX https://doi.org/XXXX/XXXX

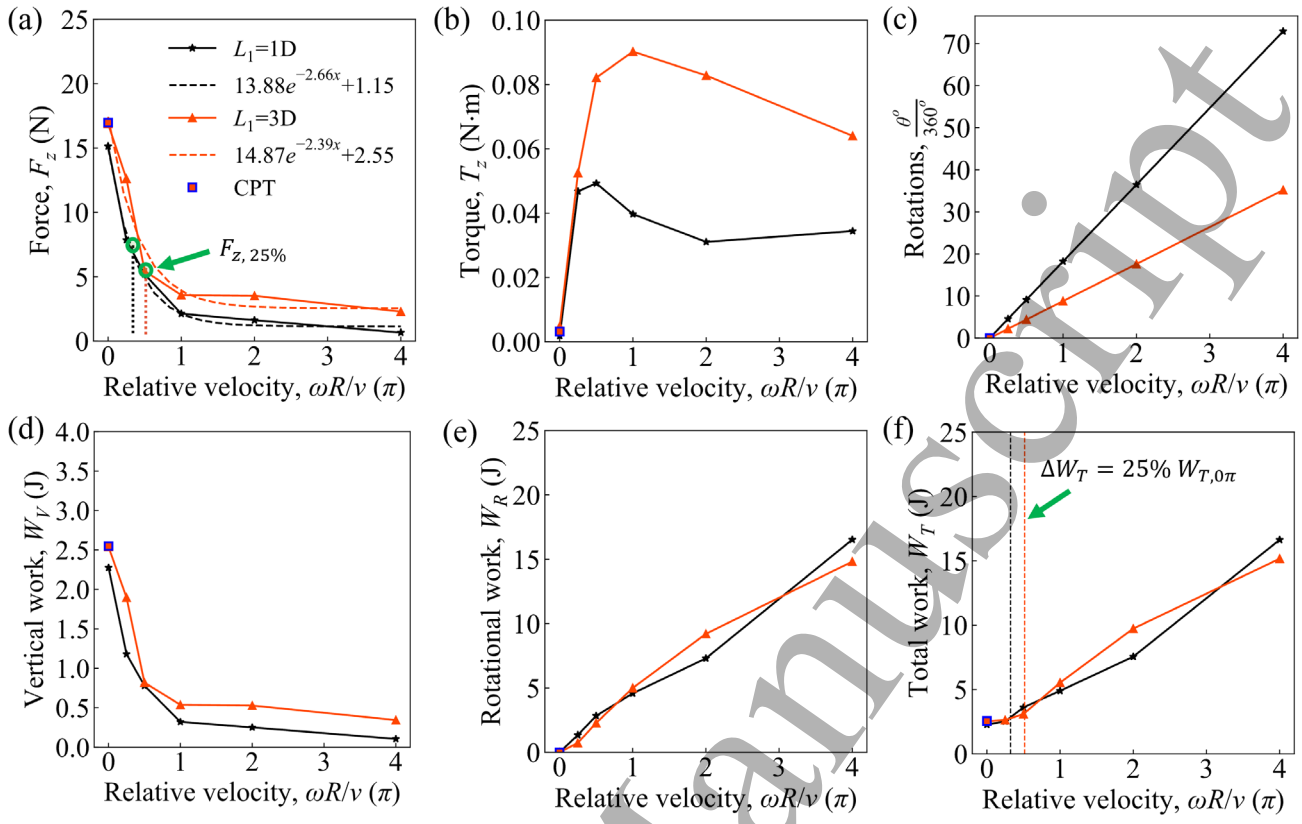

Figure 8: Effect of L_1 on variation of (a) depth-averaged vertical force, (b) depth-averaged torque, and (c) total rotational displacement; cumulative (d) vertical, (e) rotational, and (f) total work with relative velocity. Dotted lines indicating the $\omega R/v$ at which total work increases by 25% in comparison to non-rotational CIM tests are marked to highlight the extent of decay in vertical force.

between non-rotational penetration (i.e., $W_{T,0\pi}$ and $F_{z,0\pi}$) and CI penetration at an $\omega R/v$ leading to an increase of 25% in W_T (i.e., $W_{T,25\%}$), for which the corresponding F_z is mobilized (i.e., $F_{z,25\%}$). Vertical lines indicating $F_{z,25\%}$ and $W_{T,25\%}$ are included in Figures 7a and 7c, respectively, showing that for an increase in W_T of 25%, $F_{z,25\%}$ reduces to 47% of $F_{z,0\pi}$.

3.2 Effect of bent length

The bent length is varied from $1D$ to $3D$ in a series of tests to understand its effect on the penetration behavior (Table 1). In a similar manner as for the reference test set, F_z and T_z increased steadily with depth. The probe with the greater L_1 mobilized slightly higher F_z and notably higher T_z magnitudes, as shown by the depth-averaged values presented in Figures 8a and 8b. The trends with $\omega R/v$ are similar as previously described for the reference set of tests with an L_1 of $1D$. $F_{z,0\pi}$ for the probe with an L_1 of $3D$ is slightly higher than that for an L_1 of $1D$ and similar in magnitude to the F_z mobilized during a CPT.

The variation in W_V, W_R, and W_T with $\omega R/v$ for the probe with an L_1 of $3D$ follows similar trends as those of the reference test (Figures 8d-f). W_V follows the same trend as F_z, with greater W_V values for an L_1 of $3D$ than for an L_1 of $1D$ for any given $\omega R/v$. The lower rotational displacement at any given $\omega R/v$ for an L_1 of $3D$ (Figure 8c) compensates the higher T_z mobilized by this probe, resulting in W_R having similar magnitudes and variations with $\omega R/v$ (Figure 8d). This leads to the variation in W_T with $\omega R/v$ to be comparable to that of the probe with an L_1 of $1D$. At $W_{T,25\%}$, $F_{Z,25\%}$ decays to 32% of $F_{z,0\pi}$, in comparison to a corresponding decay of 47% for an L_1 of $1D$. The $\omega R/v$ at which W_T increases by 25% ($(\omega R/v)_{25\%}$) increases with increase in L_1, from 0.32 π to 0.52 π.

3.3 Effect of bent angle

The influence of the bent angle of the probe is investigated by performing sets of tests in which α is varied from 10° to either 20° or 30° (Table 1). Increasing α from 10° to 30° results in higher forces and torques at any given depth and

IOP Publishing Journal Title
Journal **XX** (XXXX) XXXXXX https://doi.org/XXXX/XXXX

$\omega R/v$, as shown by the depth-averaged values presented in Figures 9a-b. These tests show similar trends, with exponentially decaying F_z and sharp initial increases in T_z as $\omega R/v$ is increased. While F_z consistently increases with α, T_z increases as α is increased from 10° to 20° but a further increase in α to 30° resulted in no substantial change. Small deviations from expected trends may be due to variability of the T_z measurement, as described in the methods section. In addition, the $F_{z,0\pi}$ values for the probes with an α of 20° and 30° are higher than that measured in the CPT.

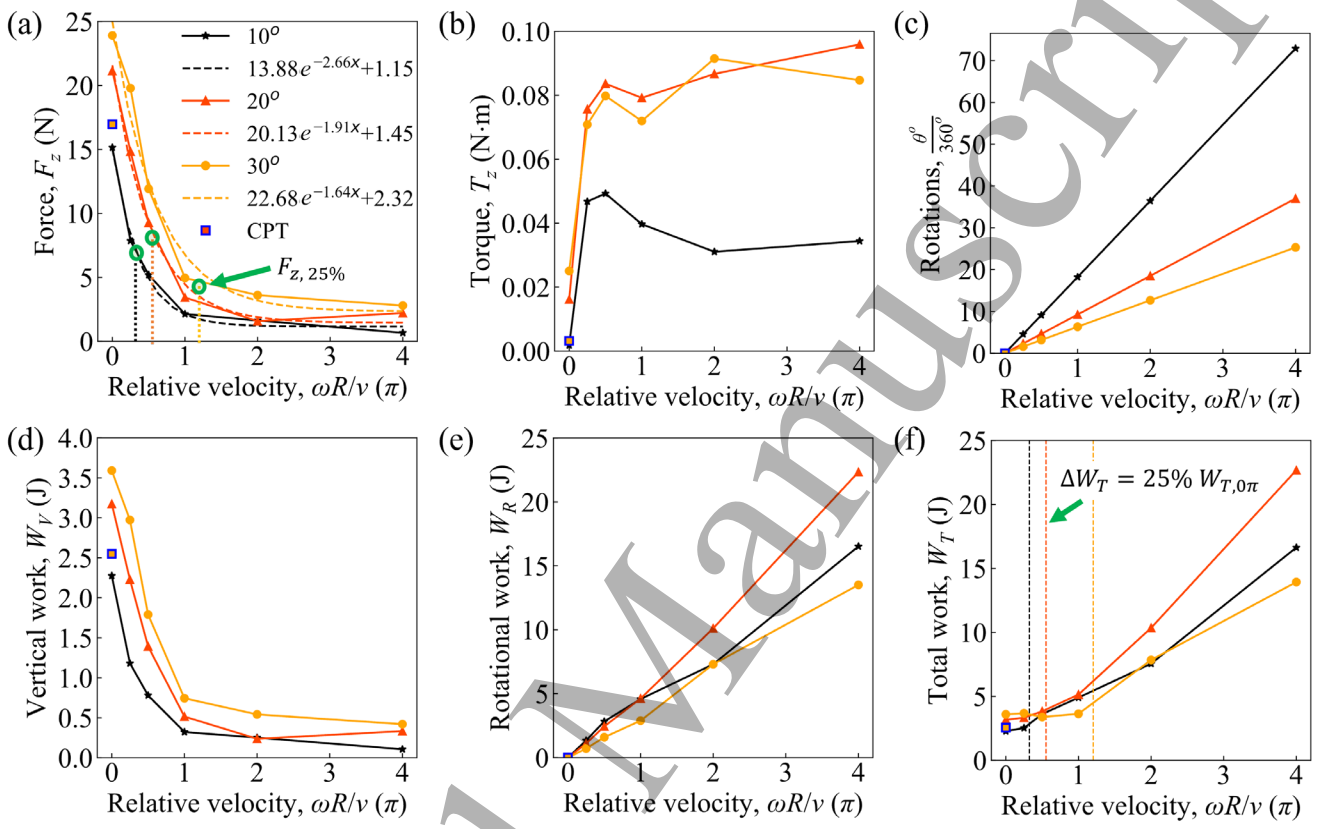

Figure 9: Effect of α on variation of (a) depth-averaged vertical force, (b) depth-averaged torque, and (c) total rotational displacement; cumulative (d) vertical, (e) rotational, and (f) total work with relative velocity. Dotted lines indicating the $\omega R/v$ at which total work increases by 25% in comparison to non-rotational CIM tests are marked to highlight the extent of decay in vertical force.

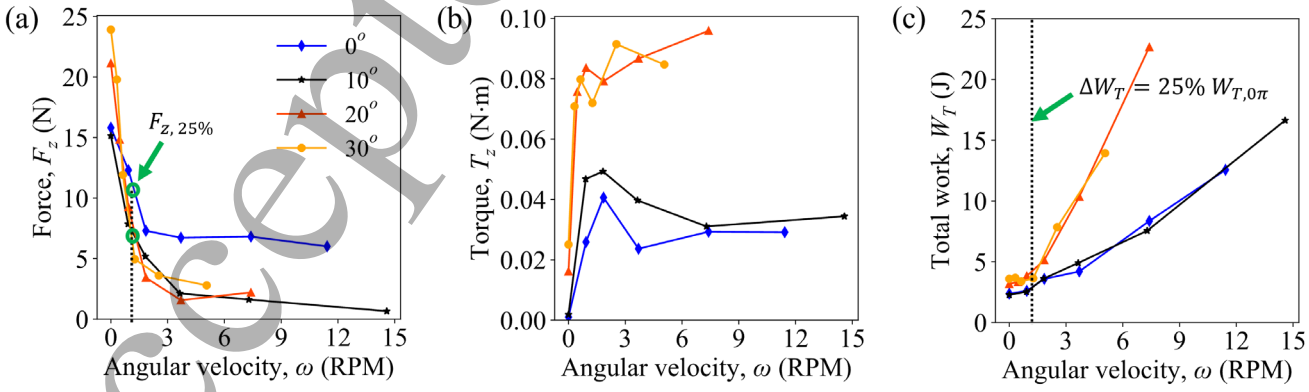

Figure 10: Variation of (a) vertical force and (b) torque with $\omega R/v$ for rotational CPT. Dotted lines indicating the $\omega R/v$ at which total work increases by 25% in comparison to non-rotational CIM tests are marked to highlight the extent of decay in vertical force.

IOP Publishing Journal Title
Journal **XX** (XXXX) XXXXXX https://doi.org/XXXX/XXXX

The work done by the probes with different α angles follow similar trends as previously described for the reference test set. Specifically, W_V decays with $\omega R/v$ in the same fashion as F_z (Figure 9d) and W_R increases monotonically with $\omega R/v$ (Figure 9e). Even though the mobilized T_z by the CI penetration probes with $\alpha = 20^o$ and 30^o are of similar magnitudes and around two times larger than that mobilized during the reference test set, the W_R for the probe with an α of 20^o is slightly higher than that for the other two probes due to the decrease in rotational displacement at the same $\omega R/v$ for probes with higher α (Figures 9c and 9e). The variation in W_T is similar for all three probes (Figure 9f). However, $(\omega R/v)_{25\%}$ increases with increase in α, from 0.32 π to 0.55 π and 1.2 π as α is increased from 10 ° to 20^o and 30^o, respectively. $F_{Z,25\%}$ decreases to 47%, 41%, and 20% of the corresponding $F_{z,0\pi}$ values for the probes with an α of 10^o, 20^o, and 30^o, respectively.

An additional set of tests was performed with an α of 0^o, meaning that the probe has no bend. The probe with an α of 0^o is treated as a special case because it has an R of zero; thus, comparison with the results of the other CI penetration probes needs to be done in terms of ω instead of $\omega R/v$. The F_z and T_z increased steadily with depth, but only depth-averaged values are presented for brevity. While F_z decays with increasing ω, this reduction in F_z is not as substantial for an α of 0^o (Figure 10a). The magnitude of T_z increases at larger extents with initial increase in ω, but yields similar magnitudes with further increases (Figure 10b). At higher ω, the T_z mobilized by the probe with α of 0^o is similar to that by the probe with α of 10^o. At an ω of 1.17 RPM (corresponding to $(\omega R/v)_{25\%}$ for the reference set of tests with an α of 10^o), the F_z mobilized are 12 N for an α of 0^o and about 7.1 N for the probes with α of 10^o, 20^o, and 30^o, as shown in Figures 10a and 8c. The smaller reduction in F_z by the probe with an α

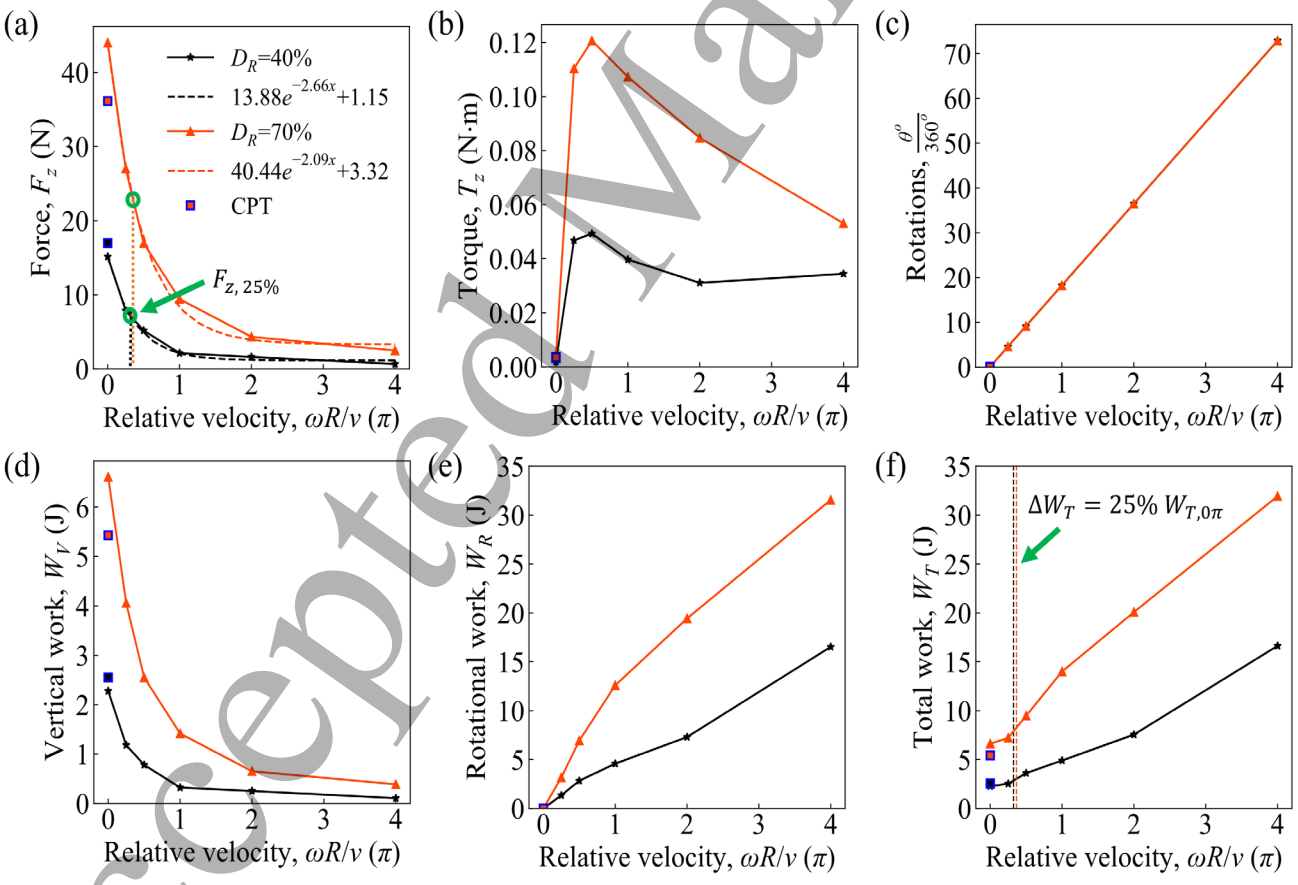

Figure 11: Effect of relative density of soil on variation of a) depth-averaged vertical force, (b) depth-averaged torque, and (c) total rotational displacement; cumulative (d) vertical, (e) rotational, and (f) total work with relative velocity. Dotted lines indicating the $\omega R/v$ at which total work increases by 25% in comparison to non-rotational CIM tests are marked to highlight the extent of decay in vertical force.

IOP Publishing Journal Title
Journal **XX** (XXXX) XXXXXX https://doi.org/XXXX/XXXX

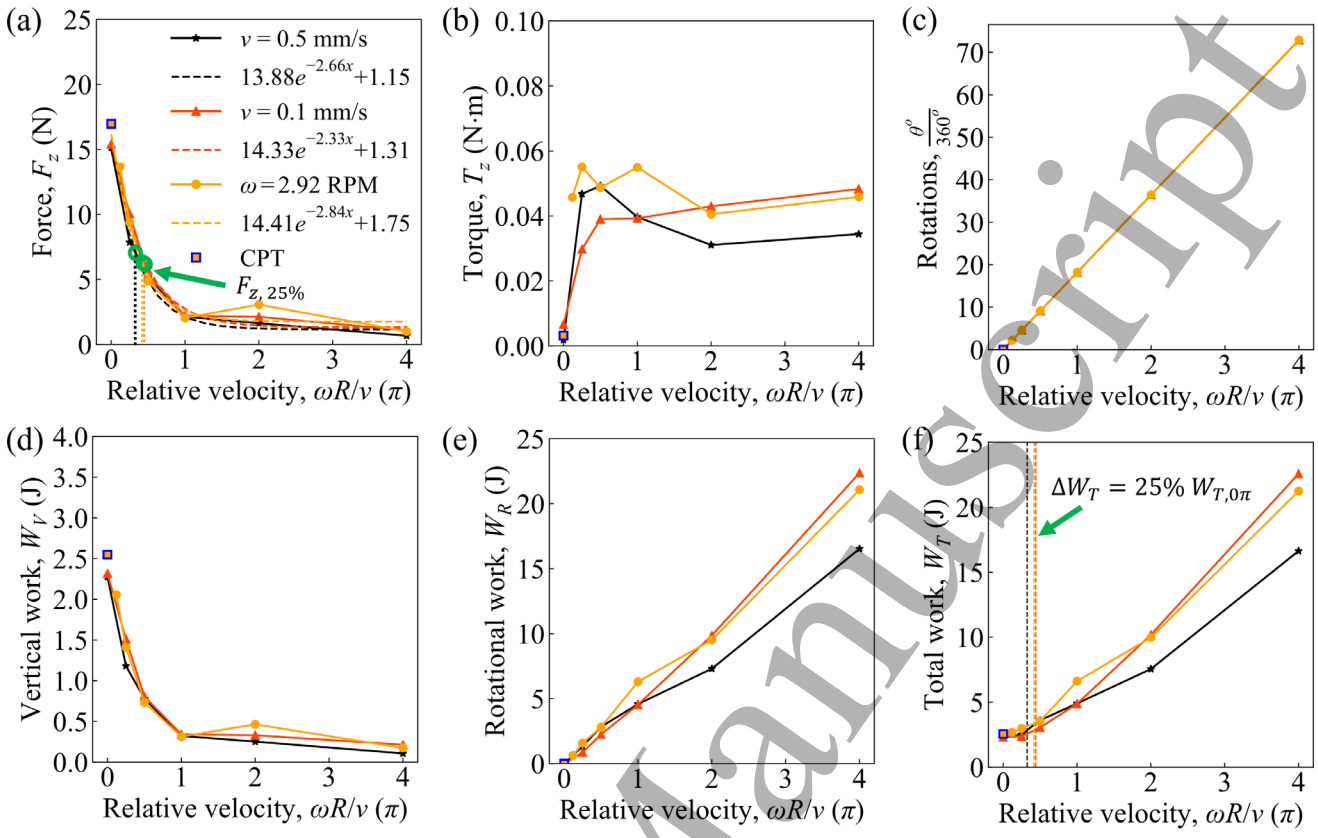

Figure 12: Effect of vertical velocity on variation of a) depth-averaged vertical force, (b) depth-averaged torque, and (c) total rotational displacement; cumulative (d) vertical, (e) rotational, and (f) total work with relative velocity. Dotted lines indicating the $\omega R/v$ at which total work increases by 25% in comparison to non-rotational CIM tests are marked to highlight the extent of decay in vertical force.

of 0° indicates that the bent tip geometry plays a significant role in the reduction of F_z.

3.4 Effect of relative density

A series of tests with a D_R of 70% was performed (Table 1). The tests on the denser soil yielded greater F_z and T_z magnitudes at any depth and $\omega R/v$, but follow similar trends as those observed in the reference tests (Figures 11a-b). The peak in the torque variation with increasing $\omega R/v$ is more prominent in the denser soil due to the greater decrease with $\omega R/v$. The $F_{z,0\pi}$ is lower than the F_z mobilized during the CPT in the loose deposit, while $F_{z,0\pi}$ is higher than that mobilized during the CPT in the dense deposit.

The work components increase with density but follow similar trends as the reference test set. Specifically, the W_V component follows the same trend as the F_z values, while the W_R monotonically increases (Figures 11d and 11e). Despite the greater W_T magnitudes for the tests on the dense soil, the $(\omega R/v)_{25\%}$ values are very similar (≈ 0.35 π) for both test series (Figure 11f), suggesting that this value is impacted only by probe geometry. In addition, the $F_{z,25\%}$ decays to a value of 51% of $F_{z,0\pi}$ in the dense deposit, showing a similar decrease as observed in the loose test set (i.e., to 47% of the corresponding $F_{z,0\pi}$).

3.5 Effect of vertical penetration velocity

The effect of v on the magnitudes of the force, torque, and work components, and their variation with $\omega R/v$, are explored by performing two additional test series: one where the v and ω were both decreased by a factor of five and a second one where ω was kept constant at 2.92 RPM while v was varied (Table 1). The depth-averaged values are presented in Figures 12a-f, which show no substantial effect of v on the variation of F_z, T_z, and W_T with $\omega R/v$. It is noted that for tests with a constant ω of 2.92 RPM, the $\omega R/v$ is never zero by definition. Therefore, the smallest

IOP Publishing Journal Title
Journal **XX** (XXXX) XXXXXX https://doi.org/XXXX/XXXX

$\omega R/v$ tested was 0.12π. While small differences are observed in the variation of T_z, which are further reflected in the variation of W_R and W_T, the magnitudes and trends are similar. The results also show that the $(\omega R/v)_{25\%}$ and $F_{z,25\%}$ values are not influenced by the penetration velocity.

4. Discussion: Variation in forces, torques, and mechanical work

This section explores the main factors governing the variation of forces, torques, and mechanical work done during CI penetration. First, the trends in the variation of the vertical force and torque are discussed and then the processes that govern these variations are explored. This is followed by a discussion on the variation of W_T and its implications on the future application of CI penetration for field tests.

4.1 Variation in penetration resistances

4.1.1 Variation in vertical penetration force. The F_z decays exponentially with increasing $\omega R/v$ for all variations of test parameters considered in this investigation. The variation of F_z with $\omega R/v$ can be described with an exponential function, as follows:

$$F_z(\omega R/v) = Ae^{-B(\omega R/v)} + C \quad (4)$$

where the constants A and C sum up to $F_{z,0\pi}$, B is the rate of decay, and C is F_z at a large $\omega R/v$. Figures 7a, 8a, 9a, 11a, and 12a provide best fits using Eq. 4 to the experimental data using Python's SciPy library to perform a non-linear least squares fit.

Comparison of the exponential fit constants and $F_{z,0\pi}$ can help better understand the effects of each of the parameters explored (Table 2). As L_1 is increased from $1D$ to $3D$, A and $F_{z,0\pi}$ increase while B decreases slightly, resulting in a higher F_z value at larger $\omega R/v$ ratio, given by C. Similar effects are observed when α is increased, which results in an increase in both A and C and a decrease in B. Increasing the relative density of the soil also results in an increase in constants A and C, which result in higher $F_{z,0\pi}$, higher F_z at large $\omega R/v$, and a decrease in B. In agreement with the results shown in Figure 12, v does not have a major effect on the A, B, and C constants.

Table 2: Vertical force decay coefficients for test sets. The parameters used in the reference test set are marked with an * indicating that the rows are identical to each other.

Parameter varied	Parameter value	A (N)	B	C (N)	$F_{z,0\pi}$ (N)
L_1	1D*	13.88	2.66	1.15	15.14
	3D	14.87	2.39	2.55	16.9
α	10°*	13.88	2.66	1.15	15.14
	20°	20.13	1.91	1.45	21.13
	30°	22.68	1.64	2.32	23.9
D_R	40%*	13.88	2.66	1.15	15.14
	70%	40.44	2.09	3.32	44.00
v	0.5 mm/s*	13.88	2.66	1.15	15.14
	0.1 mm/s	14.33	2.33	1.31	15.41
	Varying v	14.41	2.85	1.75	-

4.1.2 Variation in torque. The T_z increases with initial increases in $\omega R/v$ to a peak value ($T_{z,P}$) for all test series and then either slightly decreases or maintains constant magnitudes with further increases in $\omega R/v$. The torque at a large $\omega R/v$ (here an average between T_z at 2 π and 4 π is considered) is denoted as $T_{z,L}$, representing the value at a low helix pitch where the soil is more disturbed. Both $T_{z,P}$ and $T_{z,L}$ along with their ratio $T_{z,P}/T_{z,L}$ vary with probe geometry and D_R, as shown in Table 3. The $T_{z,P}/T_{z,L}$ ratio quantifies the decrease in T_z with increasing $\omega R/v$, which is driven by the greater soil disturbance caused by the smaller helix pitch.

The reference test series yields a $T_{z,P}/T_{z,L}$ of 1.50. Increasing α or L_1 results in increases in both $T_{z,P}$ and $T_{z,L}$, and a $T_{z,P}/T_{z,L}$ that generally decreases. The tests with a D_R of 70% show a continued decrease of T_z with $\omega R/v$, reaching a value that is slightly greater than that obtained for the reference tests on loose sand at a $\omega R/v$ of 4 π (Figure 11b). This leads to a $T_{z,P}/T_{z,L}$ value of 1.75. The $T_{z,P}$ is expected to be higher for denser soils as they mobilize higher peak shear resistance than looser soils (Holtz et al., 1981). However, at high $\omega R/v$, the soil around the probe is highly deformed, likely reaching the critical state in which the soil is completely de-structured and its shear strength is independent of the initial soil density (Mitchell and Soga, 2005). Thus, this suggests that the T_z magnitude mobilized at very large $\omega R/v$ may be independent of soil initial density.

IOP Publishing Journal Title
Journal **XX** (XXXX) XXXXXX https://doi.org/XXXX/XXXX

Table 3: Effect of test parameters on the measured torques. The parameters used in the reference test set are marked with an * indicating that the rows are identical to each other.

Parameter varied	Parameter value	$T_{z,P}$ (N.m)	$T_{z,L}$ (N.m)	$T_{z,P}/T_{z,L}$
L_1	$1D$*	0.049	0.033	1.50
	$3D$	0.09	0.073	1.23
α	10°*	0.049	0.033	1.50
	20°	0.096	0.091	1.05
	30°	0.091	0.088	1.04
D_R	40%*	0.049	0.033	1.50
	70%	0.121	0.069	1.75
v	0.5 mm/s*	0.049	0.033	1.50
	0.1 mm/s	0.048	0.046	1.06
	Varying v	0.055	0.043	1.27

4.2 Mechanisms governing the variation of penetration resistances with relative velocity

The magnitude of F_z is a complex function of the probe geometry and $\omega R/v$ because both affect the probe tip's helical trajectory, as illustrated in Figure 13a. Specifically, increasing $\omega R/v$ results in an increase of the helix angle (β). At the extremes, a β of zero corresponds to non-rotational penetration and an infinite β corresponds to purely angular displacement without a vertical component. In addition, the soil penetration resistance is greatly influenced by the soil properties (Mayne, 2014). To examine the effect of the probe tip's trajectory, a frictionless probe, such that all the resistance is originated from normal stresses between the probe and soil, with a simplified geometry can be considered, as shown in Figure 13b. For an elliptical disk element in the bent portion of the probe tip with a width of dr and located at a distance r from the axis of rotation, the resultant velocity of the element acts in some direction β_r, where $tan(\beta_r) = \omega r/v$. The resultant normal stress acting on this element is $\sigma(r)$, acting in some direction $\theta(r)$. The surface area of the probe element is dA, which is the product of dr and the perimeter of the elliptical element (with minor axis D and major axis $D/sin(\alpha)$), denoted as $f_p(D,\alpha)$. The vertical force and torque acting the element are dF_z and dT_z, respectively, given by:

$$dF_z = \sigma(r)cos(\theta(r))\, f_p(D,\alpha)\, dr \quad (5)$$
$$dT_z = \sigma(r)rsin(\theta(r))\, f_p(D,\alpha)\, dr \quad (6)$$

Since both the $\sigma(r)$ and $\theta(r)$ are unknown, the direction of resistance acting on the elliptical element can be assumed to be equal to the direction of net strain increment in the soil according to the associative flow rule. This is a common assumption in soil plasticity models which states that the direction of stress increment coincides with the direction of strain increment (Wood, 1990). Additionally, the average direction of strain increment can be taken as the direction of probe resultant velocity, which depends on r. Thus, the direction of normal stress acting on the probe is taken as $\theta(r) = \beta_r = tan^{-1}(\omega r/v)$ and the vertical force and torque contribution of any such element can be expressed as:

$$dF_z = \sigma(r)cos(\beta_r)f_p(D,\alpha)dr \quad (7)$$
$$dT_z = \sigma(r)rsin(\beta_r)f_p(D,\alpha)dr \quad (8)$$

Upon integration, these equations would yield an analytical solution of the variation of F_z and T_z with probe geometry and $\omega R/v$. However, $\sigma(r)$ is not a constant quantity, as it likely depends on r, soil type, soil density, shape of failure mechanism of the soil around the probe, and tip trajectory. The functional form of $\sigma(r)$ is unknown and could be further explored through numerical simulations to solve Eqs. (5) and (6). It is noted that analytical solutions that assume a constant $\sigma(r)$ have been developed for probes with an α of 0^o (Bengough et al., 1997); however, more recent results have shown that this assumption is not valid in soils (Chen and Martinez, 2024; Tang and Tao, 2022; Yang et al., 2024).

4.2.1 Effect of probe geometry on the projected areas and mobilized normal stresses. The effect of probe geometry on the mobilized resistance is investigated by considering the stresses acting on the projected probe areas resulting in F_z and T_z. While variations of F_z and T_z with $\omega R/v$ in different test sets have similar trends, their magnitudes increase with increases in α and L_1. Figure 14 illustrates the relevant projected areas affecting F_z and T_z for the CPT and bent CI penetration probes. The mobilized F_z is directly proportional to the probe area projected onto the horizontal plane (A_{Fz}) and the stress acting on this area. Increasing α from 10° to 30° or L_1 from $1D$ to $3D$ increases the A_{Fz} of the probe. Similarly, T_z is proportional to the projected area of the probe on a vertical plane (A_{Tz}), the stress acting on this area, and the moment arm (R_c). The A_{Tz} area is not the total projected area on the vertical plane but only the projected area of the CI probe tip that displaces soil due to the rotational motion. The R_c refers to the distance of the centroid of A_{Tz} from the axis of rotation, which increases as α and L_1 are increased. Table 4 presents the area components and moment arm for the different probe geometries calculated using a 3D modeling software.

IOP Publishing Journal Title
Journal **XX** (XXXX) XXXXXX https://doi.org/XXXX/XXXX

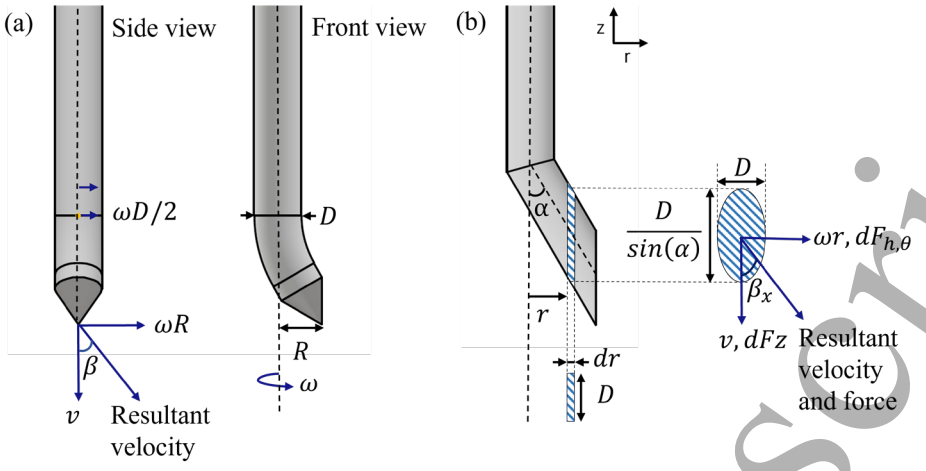

Figure 13: (a) Orthogonal views of the CI probe with diameter (D) rotated with angular velocity (ω) and vertical velocity (v). (b) Simplified probe geometry to analyze the forces acting on the probe. A vertical slice of the bent end of the probe, an elliptical element of infinitesimal thickness (dx), is illustrated.

.

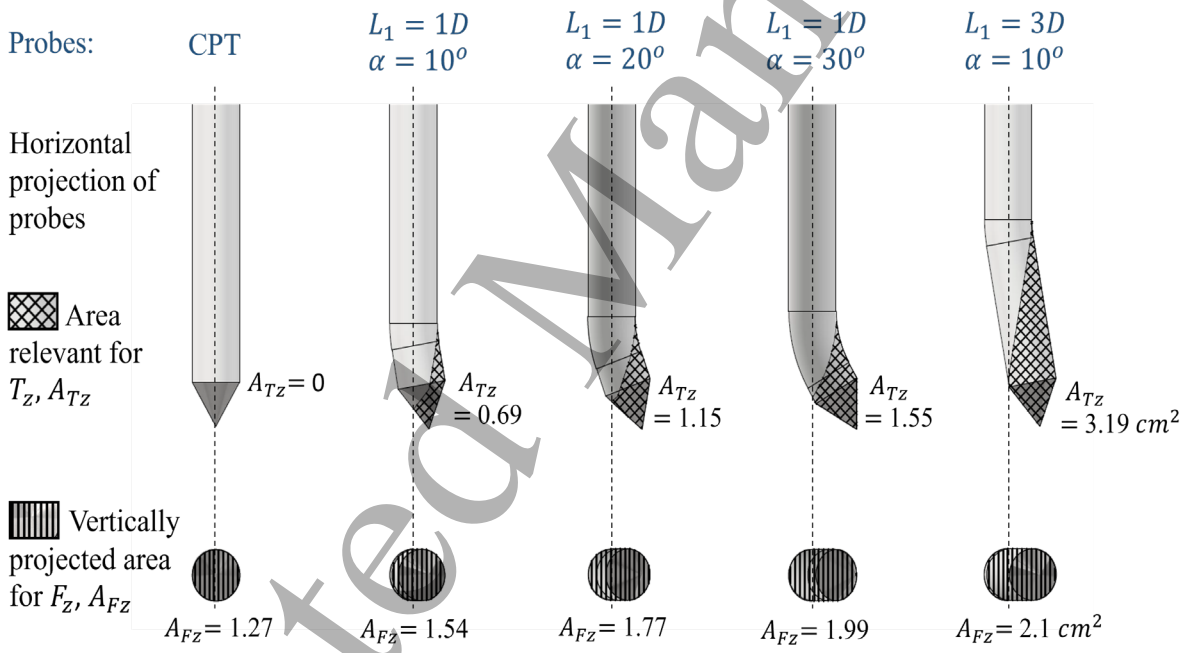

Figure 14: Horizontal and vertical projections of the probes highlighting the relevant projected areas that govern F_z and T_z.

IOP Publishing Journal Title
Journal **XX** (XXXX) XXXXXX https://doi.org/XXXX/XXXX

Table 4: Calculated projected areas, moment arms, and resultant stresses in the vertical and horizontal directions for probes in loose (D_R = 40%) and dense (D_R = 70%) sands.

Probe	A_{Fz} (cm^2)	A_{Tz} (cm^2)	R_c (cm)	σ_v (kPa)	σ_θ (kPa)
CPT, D_R = 40%	1.27	-	-	134.0	-
$L_1 = 1D$, α = 10°, D_R = 40%	1.54	0.69	0.51	98.6	15.1
$L_1 = 3D$, α = 10°, D_R = 40%	2.09	3.19	0.65	80.8	16.8
$L_1 = 1D$, α = 20°, D_R = 40%	1.77	1.16	0.62	119.1	94.0
$L_1 = 1D$, α = 30°, D_R = 40%	2.00	1.55	0.71	119.9	50.8
CPT, D_R = 70%	1.27	-	-	285.2	-
$L_1 = 1D$, α = 10°, D_R = 70%	1.54	0.69	0.51	286.6	113.9

To understand how the stresses acting on the probe change as a result of probe geometry, the resultant stresses acting on the bent tip of the probe in the vertical direction (σ_v) for non-rotational tests and in hoop direction (σ_θ) for tests at large $\omega R/v$ are calculated as follows:

$$\sigma_v = F_{z,0\pi}/A_{Fz} \quad (9)$$

$$\sigma_\theta = (T_{z,L} - T_{zL,CPT})/(R_c\, A_{Tz}) \quad (10)$$

F_z is primarily the result of stresses acting on the tip of the probe, as friction acting along the length of the probe generally has a much lower contribution for vertically penetrating probes in sands (Robertson, 1990). However, the influence of friction along the length of the probe on T_z can be substantial for probes with smaller A_{TZ}, as shown by the results of rotational CPT (0° probes). Thus, to estimate σ_θ acting on the bent tip of the probe, the difference between the $T_{z,L}$ mobilized during a given CI penetration test and that mobilized during a rotational CPT is considered. The computed stress components shown in Table 4 indicate that both σ_v and σ_θ vary with probe geometry and thus cannot be considered constant.

For a D_R of 40%, σ_v decreases and σ_θ remains near-constant as L_1 is increased. The effect of α is more complex, since an increase in angle from 0° to 10° leads to a decrease in σ_v followed by an increase with further increase in α. The σ_θ increases sharply with an increase from 10° to 20°, but it decreases with a further increase to 30° since the T_z magnitude remains constant while the area and moment arm increase (Tables 3 and 4). In addition, both stress components increase as the D_R is increased due to the increase in soil peak friction angle and dilatancy, as typically observed in CPT soundings in geotechnical site investigations (Idriss and Boulanger, 2003; Mayne, 2007). In contrast to loose sands, for dense sands the σ_v has similar magnitudes as the α angle is increased from 0° to 10°. This difference could be due to the variation in the dilative behaviour of sand with different relative densities, where dense sands dilate when they are deformed whereas loose sands contract (Mitchell and Soga, 2005). The variations in the path of soil particle displacement and failure mechanism of the soil around the tip of the probes are believed to result in the observed differences in the vertical stresses mobilized, which should be further analyzed using numerical simulations.

4.2.2 Effect of the relative velocity on the resultant stress direction. To explain the variations in F_z and T_z, a macroscopic approach can consider the increase in the hoop component of the resistive forces (F_θ) as $\omega R/v$ is increased. Since $\omega R/v$ indicates the ratio of tangential (i.e., hoop) to vertical velocity of the probe tip, greater $\omega R/v$ values lead to greater hoop components of the probe tip's velocity vector (Figure 13a). The associative flow rule assumption predicts that the direction of force increment coincides with that of strain increment, resulting in co-directionality between the resultant velocity of the probe tip and the force acting on it, as shown in Figure 13b. Therefore, a decrease in F_z and an increase in T_z are expected as $\omega R/v$ is increased if the normal stress acting on the probe were to be independent of $\omega R/v$. While this could explain the change in F_z observed in the experimental data (Figures 7a, 8a, 9a, 11a, and 12a), it does not explain the stagnation or decrease in T_z at larger $\omega R/v$ values (Figures 7b, 8b, 9b, 11b, and 12b). This supports the dependency of the normal stress acting on the probe on the relative velocity, as hypothesized in section 4.2.

4.2.3 Effect of the relative velocity on soil disturbance. Increasing the $\omega R/v$ results in a reduction in the pitch of the helical trajectory of the probe's tip, increasing the volume of soil that is displaced by the probe, as shown in Figure 15. Considering that displacing soil results in deformations in a volume that is greater than the probe's path, an increase in $\omega R/v$ (i.e., decrease in v/ω) produces an increase in the soil deformations as the zones of soil disturbance begin to overlap. Chen and Martinez (2024) performed DEM simulations that showed a greater increase in porosity, and greater reductions in mean

IOP Publishing Journal Title
Journal **XX** (XXXX) XXXXXX https://doi.org/XXXX/XXXX

effective and deviatoric stresses, as $\omega R/v$ was increased, supporting the increase in soil disturbance.

The $\omega R/v$ at which $T_{z,P}$ is mobilized is unaffected by the relative density (Figure 11b), but it varies with probe geometry. Specifically, $\omega R/v$ at $T_{z,P}$ doubled from 0.5 π to 1.0 π as the L_1 was increased from $1D$ to $3D$ (Figure 8b), while a prominent peak torque was not observed in the tests with α of 20° and 30° (Figure 9b). While $\omega R/v$ at which $T_{z,P}$ is mobilized increases with an increase in L_1, the ratio of v and ω at peak torque is not affected. The v/ω ratio or the pitch of the helical trajectory of the tip at $T_{z,P}$ is around 17 mm for both test sets. This suggests that there may exist

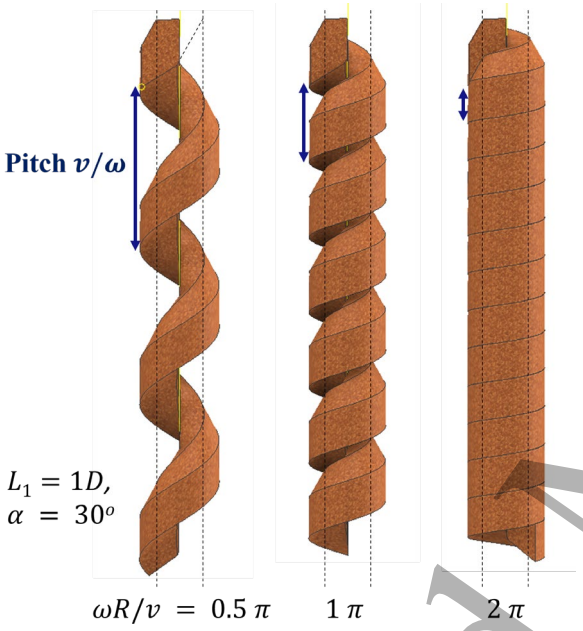

Figure 15: The variation of the CI probe tip trajectory with increasing $\omega R/v$

a critical pitch for which any smaller pitch leads to disturbance of the soil in the path of the current rotation by the previous rotations, in agreement with the results from (Guillard et al., 2013). Future investigations with larger data sets could delve into this deeper for better understanding.

4.3 Limiting total energy consumption while reducing the vertical penetration force.

The magnitude of W_T is near-constant for an initial increase in $\omega R/v$, while further increases lead to a steady increase in the total work (Figures 7c, 8f, 9f, 11f, and 12f). Here, an increase in W_T of 25% is used as a reference to denote a small but measurable increase. Vertical lines indicating the $\omega R/v$ at which W_T increases by 25% compared to the corresponding non-rotational CI penetration test ($(\omega R/v)_{25\%}$) are included in Figures 7c, 8c, 9c, 11c, and 12c. Table 5 presents the $(\omega R/v)_{25\%}$ values for the different test series, along with the F_z generated at the corresponding $(\omega R/v)_{25\%}$. The D_R and v have no measurable effect on $(\omega R/v)_{25\%}$, but the probe geometry does. Specifically, $(\omega R/v)_{25\%}$ increases as both L_1 and α are increased, with the latter parameter having a greater influence (Table 5). The $F_{z,25\%}$ magnitudes decrease as α and L_1 are increased. The $F_{z,25\%}$ values are compared with $F_{z,0\pi}$ mobilized in the same soil to understand the extent of reduction of F_z in Table 5. The results show that the $F_{z,25\%}/F_{z,0\pi}$ ratio decreases with increasing L_1 and α but is unaffected by D_R and v. These trends show that increases in α and L_1 lead to a larger range of $\omega R/v$ at which the penetration energy does not increase by a substantial amount while also mobilizing lower vertical F_z in comparison to the corresponding $F_{z,0\pi}$. However, the absolute magnitude of F_z remains lower for smaller values of L_1 and α.

The CI penetration probes with an α 10° and L_1 of $1D$ appear to be most advantageous in terms of limiting the magnitude of work done and mobilizing the smallest F_z and T_z magnitudes. Comparing the $F_{z,25\%}$ mobilized by this CI penetration probe to that vertical force during traditional CPT indicates that even with a small increase in total work of 25%, the vertical force needed to penetrate the soil can be reduced by about 63%. This indicates that there is a trade-off between the work done and vertical penetration force during soil penetration, where some applications may be limited by the energy consumption (i.e., a battery-powered device) while others may be limited by the vertical reaction force (i.e., soundings in a remote location with lightweight equipment).

Table 5: Effect of test parameters on the relative velocity at which the total work increases by 25% and the corresponding mobilized vertical penetration force. The parameters used in the reference test set are marked with an * symbol indicating that the rows are identical to each other.

Parameter varied	Parameter value	$(\omega R/v)_{25\%}$ (π)	$F_{z,25\%}$	$F_{z,25\%}/F_{z,0\pi}$
L_1	$1D$*	0.32	7.07	46.70%
	$3D$	0.52	5.38	31.90%
α	10°*	0.32	7.07	46.70%
	20°	0.55	8.65	40.90%
	30°	1.2	4.68	19.60%
D_R	40%*	0.32	7.07	46.70%
	70%	0.37	22.38	50.90%

IOP Publishing Journal Title
Journal **XX** (XXXX) XXXXXX https://doi.org/XXXX/XXXX

v	0.5 mm/s*	0.32	7.07	46.70%
	0.1 mm/s	0.44	6.45	41.80%
	Varying *v*	0.42	6.33	46.30%

5. Conclusions

This study draws inspiration from the circumnutation motions of plant roots to investigate soil penetration strategies that reduce the vertical penetration force. CI penetration probes with a bent end and conical tip were developed for this study, which were used to perform penetration tests in soil by being simultaneously rotated and inserted vertically. This investigation consisted of test series in which the effects of the relative velocity on the vertical force, torque, and work done during penetration were examined as the vertical velocity, bent angle, bent length, and sand relative density were individually varied. The broad range of probe geometries and relative velocities explored in this study have not been previously reported in literature, enhancing the understanding their effect on the mobilized resistance and work done during penetration.

In all the test sets, the F_z exponentially decayed as the $\omega R/v$ was increased, while the T_z magnitudes increased steeply with initial increases in $\omega R/v$ before reaching stable values or decreasing slightly. An increase in α and L_1 resulted in greater F_z and T_z magnitudes, while the rate of decay of F_z with $\omega R/v$ decreased as α and L_1 were increased. Variations in v did not notably influence the response, showing that $\omega R/v$ is a controlling parameter in CI soil penetration. As expected, an increase in D_R resulted in greater F_z and T_z due to the greater soil peak shear strength and increases in stresses due to soil deformation.

The variation of resistances mobilized is attributed to both the probe geometry and the $\omega R/v$ of the tests. As the α and L_1 of the probe are increased, the projected areas relevant to F_z and T_z increase, resulting in higher magnitudes. The probe geometry also influences the failure mechanism of soil around the probe and the resistive stresses mobilized. In addition to the geometry, the $\omega R/v$ of the test influences the soil failure mechanism and in turn the stresses mobilized against the probe. The decay in F_z with increasing $\omega R/v$ is attributed in part to the rotation in the direction of stresses from vertical to a more horizontal direction as $\omega R/v$ increases. This leads to resistive stress components being more horizontally oriented and lower components of resistance in the vertical direction. The plateauing of T_z with $\omega R/v$ is explained through the increasing extent of soil disturbance as $\omega R/v$ is increased, which also influences the F_z magnitudes. With increasing strains at large $\omega R/v$, the soil around the probe tip approaches its critical state after which further disturbance creates no change in the resistance mobilized.

The W_V follows the same exponentially decaying trend with $\omega R/v$ as F_z. In contrast, W_R steadily increases with $\omega R/v$. W_T, being the sum W_V and W_R, has near-constant values at low values of $\omega R/v$ while additional increments produce a steady increase for all the test sets. This indicates that for a range of low $\omega R/v$, the absolute rate of change in W_V and W_R is similar. Since F_z decays exponentially with $\omega R/v$, the upper limit of this range can be used to minimize F_z mobilized while limiting the total energy consumed.

The CI penetration probe with an α of 10° and L_1 of $1D$ may be the most advantageous design considered in this investigation for minimizing F_z and limiting the increase in W_T. When W_T is increased by 25% with respect to traditional CPT, the vertical reaction forces for this probe are reduced by about 63%. While at higher $\omega R/v$ of 2π to 4π the vertical penetration force can be reduced by a factor of up to ten, the total work done can increase substantially.

The significant reduction in vertical resistance observed during CI penetration could allow for the use of smaller, lightweight penetration equipment which would lower the mobilization costs and carbon footprint of field testing equipment and increase the accessibility to remote or congested sites. However, additional accommodations may be required for the penetration equipment to provide sufficient reaction torque. Further investigation on the effect of wider range of probe geometries, soil type, depth, and confining stress on the forces, torques, and work components involved in CI penetration, along with considerations of possible integration with existing equipment, is necessary to facilitate future advancements in this area.

Acknowledgements

The authors express their gratitude to undergraduate students Fabian Zamora, Junhan Li, Breiner Rodas, Davis Kim, and Rosemary Reuter for their help in the preparation of the sand deposit. Additionally, the authors extend their appreciation to the faculty and staff at the Center for Geotechnical Modeling (CGM), UC Davis, for their invaluable support, which played a crucial role in making the experimental setup feasible.

This material is based upon work supported by the National Science Foundation (NSF) under Award No. 1942369 and the Engineering Research Center Program of the NSF under NSF Cooperative Agreement No. EEC–1449501. Any opinions, findings, and conclusions or recommendations expressed in this material are those of the author(s) and do not necessarily reflect those of the NSF.

IOP Publishing Journal Title
Journal **XX** (XXXX) XXXXXX https://doi.org/XXXX/XXXX

References

Abdoun, T., Danisch, L., Ha, D., 2005. Advanced sensing for real-time monitoring of geotechnical systems, in: Site Characterization and Modeling. pp. 1–10.

Bengough, A.G., Mackenzie, C.J., Elangwe, H.E., 1994. Biophysics of the growth responses of pea roots to changes in penetration resistance. Plant Soil 167, 135–141. https://doi.org/10.1007/BF01587608

Bengough, A.G., Mullins, C.E., Wilson, G., 1997. Estimating soil frictional resistance to metal probes and its relevance to the penetration of soil by roots. Eur. J. Soil Sci. 48, 603–612. https://doi.org/10.1111/j.1365-2389.1997.tb00560.x

Bolton, M.D., Gui, M.W., Garnier, J., Corte, J.F., Bagge, G., Laue, J., Renzi, R., 1999. Centrifuge cone penetration tests in sand. Géotechnique 49, 543–552. https://doi.org/10.1680/geot.1999.49.4.543

Boulanger, R.W. and DeJong, J.T., 2018. Inverse filtering procedure to correct cone penetration data for thin-layer and transition effects. In Cone penetration testing 2018 (pp. 25-44). CRC Press.

Campbell, D.J., O'Sullivan, M.F., 1991. The cone penetrometer in relation to trafficability, compaction, and tillage. Soil Anal. Phys. Methods Marcel Dekker Inc N. Y. NY 1991 P 399-429 10 Fig 1 Tab 82 Ref.

Chen, Y., Khosravi, A., Martinez, A., DeJong, J., 2021. Modeling the self-penetration process of a bio-inspired probe in granular soils. Bioinspir. Biomim. 16, 046012. https://doi.org/10.1088/1748-3190/abf46e

Chen, Y., Martinez, A., 2024. DEM modelling of root circumnutation-inspired penetration in shallow granular materials. Géotechnique 1–18. https://doi.org/10.1680/jgeot.22.00258

Darwin, C., Darwin, S.F., 1880. The Power of Movement in Plants. John Murray.

Davidson, D.T., 1965. Penetrometer Measurements, in: Methods of Soil Analysis. John Wiley & Sons, Ltd, pp. 472–484. https://doi.org/10.2134/agronmonogr9.1.c37

Del Dottore, E., Mondini, A., Sadeghi, A., Mattoli, V., Mazzolai, B., 2017. An efficient soil penetration strategy for explorative robots inspired by plant root circumnutation movements. Bioinspir. Biomim. 13, 015003. https://doi.org/10.1088/1748-3190/aa9998

Dorgan, K.M., 2018. Kinematics of burrowing by peristalsis in granular sands. J. Exp. Biol. jeb.167759. https://doi.org/10.1242/jeb.167759

Dorgan, K.M., Jumars, P.A., Johnson, B., Boudreau, B.P., Landis, E., 2005. Burrow extension by crack propagation. Nature 433, 475–475. https://doi.org/10.1038/433475a

Dorgan, K.M., Law, C.J., Rouse, G.W., 2013. Meandering worms: mechanics of undulatory burrowing in muds. Proc. R. Soc. B Biol. Sci. 280, 20122948. https://doi.org/10.1098/rspb.2012.2948

Gidmark, N.J., Strother, J.A., Horton, J.M., Summers, A.P., Brainerd, E.L., 2011. Locomotory transition from water to sand and its effects on undulatory kinematics in sand lances (Ammodytidae). J. Exp. Biol. 214, 657–664. https://doi.org/10.1242/jeb.047068

Guillard, F., Forterre, Y., Pouliquen, O., 2013. Depth-Independent Drag Force Induced by Stirring in Granular Media. Phys. Rev. Lett. 110, 138303. https://doi.org/10.1103/PhysRevLett.110.138303

Guireli Netto, L., Barbosa, A.M., Galli, V.L., Pereira, J.P.S., Gandolfo, O.C.B., Birelli, C.A., 2020. Application of invasive and non-invasive methods of geo-environmental investigation for determination of the contamination behavior by organic compounds. J. Appl. Geophys. 178, 104049. https://doi.org/10.1016/j.jappgeo.2020.104049

Holtz, R.D., Kovacs, W.D., Sheahan, T.C., 1981. An introduction to geotechnical engineering. Prentice-Hall Englewood Cliffs.

Huang, A.-B., Ma, M.Y., 1994. An analytical study of cone penetration tests in granular material. Can. Geotech. J. 31, 91–103. https://doi.org/10.1139/t94-010

Huang, S., Tao, J., 2020. Modeling Clam-inspired Burrowing in Dry Sand using Cavity Expansion Theory and DEM. Acta Geotech. 15, 2305–2326. https://doi.org/10.1007/s11440-020-00918-8

Idriss, I., Boulanger, R.W., 2003. Relating Kα and Kσ to SPT blow count and to CPT tip resistance for use in evaluating liquefaction potential. Presented at the Proc. of the 2003 Dam Safety Conference, pp. 7–10.

Jamiolkowski, M., Lo Presti, D.C.F., Manassero, M., 2012. Evaluation of Relative Density and Shear Strength of Sands from CPT and DMT 201–238. https://doi.org/10.1061/40659(2003)7

Kim, H., Kobayashi, A., Fujii, N., Miyazawa, Y., Takahashi, H., 2016. Gravitropic response and circumnutation in pea (Pisum sativum) seedling roots. Physiol. Plant. 157, 108–118. https://doi.org/10.1111/ppl.12406

Kiss, J.Z., 2009. Plants circling in outer space. New Phytol. 182, 555–557. https://doi.org/10.1111/j.1469-8137.2009.02817.x

Kudrolli, A., Ramirez, B., 2019. Burrowing dynamics of aquatic worms in soft sediments. Proc. Natl. Acad. Sci. U. S. A. 116, 25569–25574. https://doi.org/10.1073/pnas.1911317116

Loshchilov, I., Dottore, E.D., Mazzolai, B., Floreano, D., 2021. Conditions for the emergence of

circumnutations in plant roots. PLOS ONE 16, e0252202. https://doi.org/10.1371/journal.pone.0252202

Maladen, R.D., Ding, Y., Li, C., Goldman, D.I., 2009. Undulatory swimming in sand: subsurface locomotion of the sandfish lizard. Science 325, 314–318. https://doi.org/10.1126/science.1172490

Martinez, A., Dejong, J., Akin, I., Aleali, A., Arson, C., Atkinson, J., Bandini, P., Baser, T., Borela, R., Boulanger, R., Burrall, M., Chen, Y., Collins, C., Cortes, D., Dai, S., DeJong, T., Del Dottore, E., Dorgan, K., Fragaszy, R., Frost, J.D., Full, R., Ghayoomi, M., Goldman, D.I., Gravish, N., Guzman, I.L., Hambleton, J., Hawkes, E., Helms, M., Hu, D., Huang, L., Huang, S., Hunt, C., Irschick, D., Lin, H.T., Lingwall, B., Marr, A., Mazzolai, B., McInroe, B., Murthy, T., O'Hara, K., Porter, M., Sadek, S., Sanchez, M., Santamarina, C., Shao, L., Sharp, J., Stuart, H., Stutz, H.H., Summers, A., Tao, J., Tolley, M., Treers, L., Turnbull, K., Valdes, R., Van Paassen, L., Viggiani, G., Wilson, D., Wu, W., Yu, X., Zheng, J., 2022. Bio-inspired geotechnical engineering: principles, current work, opportunities and challenges. Géotechnique 72, 687–705. https://doi.org/10.1680/jgeot.20.P.170

Martinez, A., DeJong, J.T., Jaeger, R.A., Khosravi, A., 2020. Evaluation of self-penetration potential of a bio-inspired site characterization probe by cavity expansion analysis. Can. Geotech. J. 57, 706–716. https://doi.org/10.1139/cgj-2018-0864

Mayne, P., 2014. Interpretation of geotechnical parameters from seismic piezocone tests. Presented at the Proceedings, 3rd international symposium on cone penetration testing, pp. 47–73.

Mayne, P.W., 2007. Cone penetration testing. Transportation Research Board.

Migliaccio, F., Tassone, P., Fortunati, A., 2013. Circumnutation as an autonomous root movement in plants. Am. J. Bot. 100, 4–13. https://doi.org/10.3732/ajb.1200314

Millar, K.D.L., Johnson, C.M., Edelmann, R.E., Kiss, J.Z., 2011. An Endogenous Growth Pattern of Roots Is Revealed in Seedlings Grown in Microgravity. Astrobiology 11, 787–797. https://doi.org/10.1089/ast.2011.0699

Mitchell, J.K., Soga, K., 2005. Fundamentals of soil behavior. John Wiley & Sons New York.

Moraes, M.T. de, Silva, V.R. da, Zwirtes, A.L., Carlesso, R., 2014. Use of penetrometers in agriculture: a review. Eng. Agríc. 34, 179–193. https://doi.org/10.1590/S0100-69162014000100019

Mullen, J.L., Turk, E., Johnson, K., Wolverton, C., Ishikawa, H., Simmons, C., Söll, D., Evans, M.L., 1998. Root-Growth Behavior of the Arabidopsis Mutant *rgr1*. Plant Physiol. 118, 1139–1145. https://doi.org/10.1104/pp.118.4.1139

Naziri, S., Cortes, D.D., Ridgeway, C., Ibarra, S., Provenghi, K., Castelo, J.A., 2021. Bioinspired Regolith Penetration Probe for Lunar Exploration, in: ASCEND 2021, ASCEND. American Institute of Aeronautics and Astronautics. https://doi.org/10.2514/6.2021-4156

Popova, L., Russino, A., Ascrizzi, A., Mazzolai, B., 2012. Analysis of movement in primary maize roots. Biologia (Bratisl.) 67, 517–524. https://doi.org/10.2478/s11756-012-0023-z

Purdy, C.M., Raymond, A.J., DeJong, J.T., Kendall, A., Krage, C., Sharp, J., 2022. Life-cycle sustainability assessment of geotechnical site investigation. Can. Geotech. J. 59, 863–877. https://doi.org/10.1139/cgj-2020-0523

Raymond, A.J., Tipton, J.R., Kendall, A., DeJong, J.T., 2020. Review of impact categories and environmental indicators for life cycle assessment of geotechnical systems. J. Ind. Ecol. 24, 485–499. https://doi.org/10.1111/jiec.12946

Robertson, P.K., 1990. Soil classification using the cone penetration test. Can. Geotech. J. 27, 151–158.

Robinson, D.A., Campbell, C.S., Hopmans, J.W., Hornbuckle, B.K., Jones, S.B., Knight, R., Ogden, F., Selker, J., Wendroth, O., 2008. Soil Moisture Measurement for Ecological and Hydrological Watershed-Scale Observatories: A Review. Vadose Zone J. 7, 358–389. https://doi.org/10.2136/vzj2007.0143

Sadeghi, A., Tonazzini, A., Popova, L., Mazzolai, B., 2014. A Novel Growing Device Inspired by Plant Root Soil Penetration Behaviors. PLoS ONE 9, e90139. https://doi.org/10.1371/journal.pone.0090139

Schmertmann, J.H., Palacios, A., 1979. Energy Dynamics of SPT. J. Geotech. Eng. Div. 105, 909–926. https://doi.org/10.1061/AJGEB6.0000839

Shillaber, C.M., Mitchell, J.K., Dove, J.E., 2014. Assessing Environmental Impacts in Geotechnical Construction: Insights from the Fuel Cycle 3516–3525. https://doi.org/10.1061/9780784413272.341

Shin, H., Santamarina, J.C., 2011. Open-mode discontinuities in soils. Géotechnique Lett. 1, 95–99. https://doi.org/10.1680/geolett.11.00014

Simmons, C., Söll, D., Migliaccio, F., 1995. Circumnutation and gravitropism cause root waving in Arabidopsis thaliana. J. Exp. Bot. 46, 143–150. https://doi.org/10.1093/jxb/46.1.143

Simons, N., Menzies, B., Matthews, M., 2002. A short course in geotechnical site investigation. Thomas Telford.

Tang, Y., Tao, J., 2022. Multiscale analysis of rotational penetration in shallow dry sand and implications for self-burrowing robot design. Acta Geotech. https://doi.org/10.1007/s11440-022-01492-x

Taylor, I., Lehner, K., McCaskey, E., Nirmal, N., Ozkan-Aydin, Y., Murray-Cooper, M., Jain, R., Hawkes, E.W., Ronald, P.C., Goldman, D.I., Benfey, P.N., 2021. Mechanism and function of root circumnutation. Proc. Natl. Acad. Sci. U. S. A. 118, e2018940118. https://doi.org/10.1073/pnas.2018940118

Trueman, E., 1967. The dynamics of burrowing in Ensis (Bivalvia). Proc. R. Soc. Lond. B Biol. Sci. 166, 459–476.

Vaid, Y.P., Negussey, D., 1988. Preparation of reconstituted sand specimens, in: Advanced Triaxial Testing of Soil and Rock. ASTM International.

Wan, M.S., Standing, J.R., 2014. Lessons learnt from installation of field instrumentation. Proc. Inst. Civ. Eng.-Geotech. Eng. 167, 491–506.

Winter, A.G., Hosoi, A.E., 2011. Identification and Evaluation of the Atlantic Razor Clam (Ensis directus) for Biologically Inspired Subsea Burrowing Systems. Integr. Comp. Biol. 51, 151–157. https://doi.org/10.1093/icb/icr038

Wood, D.M., 1990. Soil Behaviour and Critical State Soil Mechanics. Cambridge University Press.

Yang, X., Zhang, N., Wang, R., Martinez, A., Chen, Y., Fuentes, R., Zhang, J.-M., 2024. A numerical investigation on the effect of rotation on the Cone Penetration Test. Can. Geotech. J.

